Chemical Science

ROYAL SOCIETY OF CHEMISTRY

EDGE ARTICLE

View Article Online
View Journal

Cite this: DOI: 10.1039/d5sc06755c

All publication charges for this article have been paid for by the Royal Society of Chemistry

Designing wide-spectrum-responsive cathode catalysts with abundant active sites for high-performance photo-enabled lithium–oxygen batteries *via* band engineering

Yanhui Gan,†[a] Min Yue,†[a] Yujia Niu,[a] Chengjie Wu,[a] Songtao Zhang,[d] Mengtao Ma,[a] Hao Gong,*[a] Hairong Xue*[bc] and Renzhi Ma*[e]

Aprotic lithium–oxygen batteries (LOBs) have been regarded as novel energy storage devices due to their excellent specific energy density, yet the large discharge/charge overpotentials remain a formidable obstacle to be overcome. A photoassisted battery has been verified as one of the most effective approaches to reduce the overpotentials of LOBs. Herein, ZnO nanorod arrays were *in situ* grown on carbon textile, followed by *in situ* transformation to form Zn-HHTP@ZnO (HHTP, hexahydroxytriphenylene) heterojunction photocatalysts. The porous structure and conjugated system of highly conductive Zn-HHTP provide efficient electron conduction pathways, compensating for the insufficient conductivity of ZnO. The nano-array structure enables multiple scattering and reflection of incident light within the array, enhancing photon utilization efficiency. The *in situ* grown Zn-HHTP@ZnO heterojunction composite not only possesses abundant active catalytic sites but also exhibits a broad light absorption range. Consequently, the assembled LOBs with Zn-HHTP@ZnO cathode deliver a low charging potential of 3.20 V under illumination and an excellent energy efficiency of 93.4%, which is significantly higher than that of 78% under dark conditions. Therefore, this paper provides a deeper understanding of the mechanism of photoexcited charge carriers in LOBs and will facilitate further exploration of light-involved energy storage systems.

Received 2nd September 2025
Accepted 8th December 2025

DOI: 10.1039/d5sc06755c

rsc.li/chemical-science

Instructions

With the increasing consumption of fossil fuels and the development of electric vehicles, there is an urgent need to develop low-cost, environmentally friendly, and efficient energy conversion systems.[1–6] Lithium–oxygen (Li–O_2) batteries stand out as leading candidates among storage batteries due to their remarkable theoretical energy density (3500 Wh kg^{-1}).[7,8] However, they are hindered by several unresolved technical challenges, including low round-trip efficiency, poor rate capability, and inferior cycle stability resulting from the sluggish kinetics of oxygen reduction (ORR) and evolution (OER) reactions.[9–12] To achieve high reversibility in lithium–oxygen batteries (LOBs), effective bifunctional electrocatalysts have been widely reported to promote ORR and OER. Nevertheless, inherent issues such as the insulating nature of discharge products still lead to high charging overpotentials. The introduction of photoassisted Li–O_2 batteries has proven to be an effective strategy for achieving high performance, featuring enhanced reaction kinetics and low energy barriers,[13–15] which largely depends on the development of semiconductor photoelectrodes. These photoelectrodes possess the capability to generate highly active electrons and holes by capturing photons. Considerable research efforts have been dedicated to the rational design of photoanode catalysts to expand the limited utilization of solar energy and suppress the recombination of photogenerated electron–hole pairs.[16,17]

Yu *et al.*[18] combined the mechanism of dye-sensitized batteries with LOBs and fabricated the original photoassisted LOBs. In detail, the discharge products (Li_2O_2) are formed on the porous oxygen cathode, while the generated holes from another TiO_2 photoelectrode will oxidize the I-, which further reacts with Li_2O_2. After that, several semiconducting cathodes were applied for oxidation of Li_2O_2 to reduce the charging overpotential. The photogenerated charge carriers can not only

[a]*Department of Chemistry and Materials Science, College of Science, Nanjing Forestry University, Nanjing 210037, P. R. China. E-mail: gonghao@njfu.edu.cn*

[b]*Zhongyuan Critical Metals Laboratory, Zhengzhou University, Zhengzhou, 450001, P. R. China. E-mail: xuehairong@zzu.edu.cn*

[c]*State Key Laboratory of Critical Metals Beneficiation, Metallurgy and Purification, Zhengzhou 450001, P. R. China*

[d]*Testing Center, Yangzhou University, Yangzhou 225009, P. R. China*

[e]*Research Center for Materials Nanoarchitectonics, National Institute for Materials Science (NIMS), 1-1 Namiki, Tsukuba, Ibaraki 305-0044, Japan. E-mail: MA.Renzhi@nims.go.jp*

† Yanhui Gan and Min Yue contributed equally to this work.

enhance the oxidation reaction but also promote the reduction reaction.[19] Recently, Zhou *et al.*[20] reported that doping Ru into the interstitial sites of β-MnO_2 induces lattice expansion, introduces additional reaction sites, enhances light absorption, and accelerates redox reaction kinetics. The assembled photo-assisted LOBs achieve a cycle efficiency as high as 98.4%, excellent high-rate performance, and outstanding cycle stability exceeding 720 hours. Li *et al.*[21] developed a novel porphyrin-based metal–organic framework, which enables efficient dissociation of excited-state electron–hole pairs (excitons) through precise regulation of metal–oxygen clusters, thus promoting the generation of photogenerated charge carriers. This scheme not only significantly improves the charge–discharge efficiency of the battery but also reduces the overall overpotential, achieving an energy conversion efficiency of up to 92.0%. Despite the current development of various photo-assisted Li–O_2 battery designs, issues such as limited light absorption capacity, low photon utilization efficiency, and sluggish reaction kinetics still restrict the photoelectric conversion efficiency and battery performance.[22,23] The band structure is an intrinsic determinant of photocatalytic performance, and band engineering serves as the core technique for regulating the electronic structure of semiconductor materials, particularly the positions of the conduction band minimum and valence band maximum, and the bandgap width. Band engineering can optimize photocatalytic behavior by regulating the band structure, making it an effective approach to address the aforementioned photocatalytic challenges in the design of photoassisted Li–O_2 batteries. Although heterojunctions can be constructed *via* band engineering to enhance the light absorption of materials, Schottky barriers and ohmic resistances at traditional two-phase interfaces still hinder electron–hole diffusion.

Here, ZnO nanorod arrays were *in situ* grown on carbon textile as shown in Fig. 1a, followed by *in situ* transformation to form Zn-HHTP@ZnO heterojunction photocatalysts. Compared with conventional TiO_2, ZnO offers several notable advantages as a photocatalyst. Its slightly narrower bandgap and higher conduction band position endow ZnO with stronger reduction capability and broader light absorption. Moreover, the Zn–O bonds in ZnO possess greater covalent character and enhanced electron cloud overlap, facilitating efficient electron transport within the lattice. In contrast, TiO_2 exhibits more ionic Ti–O bonding, which leads to stronger electron confinement and increased lattice and defect scattering, thereby impeding charge migration. In addition, ZnO can be readily synthesized into diverse nanostructures and forms stable interfaces with other semiconductors, enabling the efficient construction of heterojunctions. However, ZnO can only absorb light in the ultraviolet region. As a narrow-bandgap semiconductor, Zn-HHTP is capable of absorbing photons within the visible light range. Through heteroepitaxial growth, it forms an intimate interfacial contact with ZnO nanorods, resulting in the *in situ* construction of a well-coupled heterojunction. This heterojunction integrates the band structure characteristics of both ZnO and Zn-HHTP, allowing the Zn-HHTP@ZnO composite to achieve a band alignment that covers the entire ultraviolet–visible light region. Furthermore, the π–π transition characteristics of the HHTP ligand further broaden the absorption range toward longer-wavelength visible light. Consequently, combining ZnO with

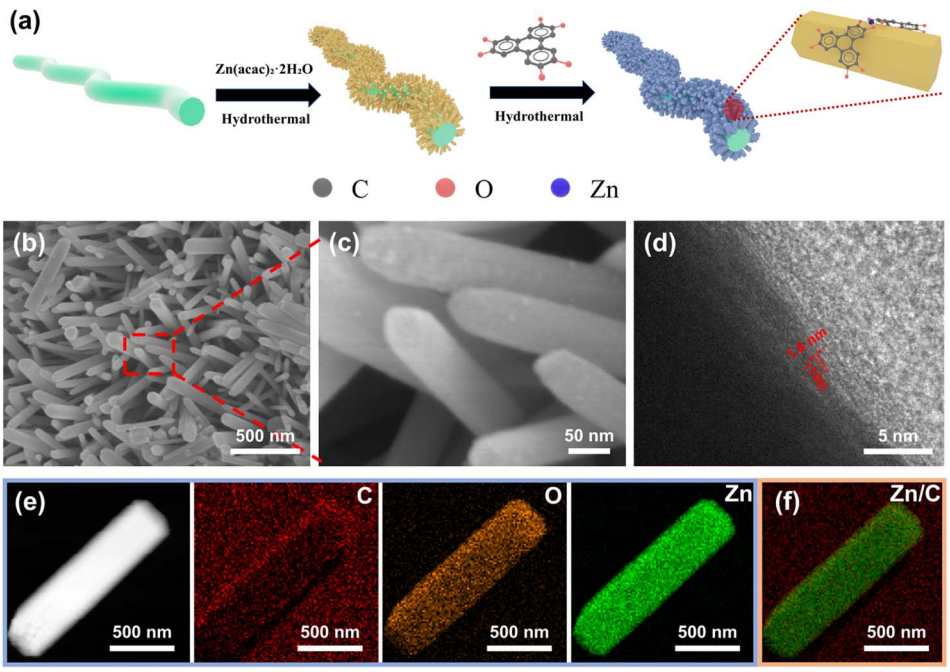

Fig. 1 (a) Synthesis schematic of Zn-HHTP@ZnO. (b and c) SEM images of Zn-HHTP@ZnO. (d) High-resolution transmission electron microscopy (TEM) image. (e) TEM image of the Zn-HHTP@ZnO sample and the mapping results of C, O and Zn. (f) Schematic diagram of the mapping overlay of Zn and C.

a narrow-bandgap semiconductor through rational band engineering enables the realization of full-spectrum light absorption in ZnO. The nano-array structure enables multiple scattering and reflection of incident light within the array, enhancing photon utilization efficiency. The porous structure and conjugated system of highly conductive Zn-HHTP provide efficient electron conduction pathways, compensating for the insufficient conductivity of ZnO. For one thing, upon light illumination, ultraviolet light excites ZnO semiconductors to generate electron–hole pairs, which rapidly migrate through the heterojunction surface to Zn-HHTP to participate in redox reactions. During discharge, numerous photoexcited electrons act as reaction sites to promote the reduction of O_2 to LiO_2, which eventually deposits as Li_2O_2. During charging, photogenerated holes in the valence band directly oxidize Li_2O_2 due to their high oxidizability, helping to reduce the oxidation potential of Li_2O_2 during charging.[24] The *in situ* Zn-HHTP and ZnO composite has a tight interfacial layer; photocarriers are generated on the surface, and photogenerated electrons in the conduction band can be rapidly transferred through the Zn-HHTP layer to the interface to participate in oxygen reduction reactions. Besides, the narrow band structure of Zn-HHTP ensures visible light absorption, endowing the Zn-HHTP@ZnO composite with a broad light absorption range and high photoelectric conversion efficiency. As a cocatalyst, Zn-HHTP has abundant catalytic sites, enabling faster redox reactions. The assembled battery demonstrates a high discharge potential of 3.00 V and a low charging potential of 3.20 V, with a narrow overpotential of only 200 mV and an energy efficiency as high as 93.4%.

Results and discussion

The Zn-HHTP@ZnO nanoarray structure was constructed on a flexible carbon textile substrate *via* multiple liquid-phase deposition steps, as shown in Fig. 1a. First, the ZnO seed layer was pre-deposited on the carbon textile surface as a growth template.[25,26] The carbon textile was then vertically placed in a reaction kettle for hydrothermal reaction to induce the oriented growth of ZnO nanorods.[27–30] The structure was solidified by heat treatment to improve crystal stability. After that, the ZnO nanorods were partially dissolved in a weakly acidic solution and served as a sacrificial template, providing a Zn source for the direct growth of Zn-HHTP, thereby forming a well-arranged and structurally stable Zn-HHTP@ZnO composite.[31]

The morphology of the obtained Zn-HHTP@ZnO and ZnO samples was first observed by SEM and TEM. As exhibited in Fig. 1b, c and S1a, the Zn-HHTP@ZnO nanorod arrays presented a closely ordered vertical growth morphology on the flexible carbon textile surface, with a distinct rounded morphology at the nanorod ends. In contrast, the original ZnO nanorods had a typical hexagonal prism structure, as shown in Fig. S1b and c. The morphological changes confirmed that ZnO nanorods are etched and effectively coated with Zn-HHTP. The HR-TEM image of Zn-HHTP@ZnO is given in Fig. 1d, where regular lattice fringes with a spacing of 1.8 nm, matching the (100) crystal plane spacing of Zn-HHTP, confirm the successful composite of Zn-HHTP on the surface of ZnO nanorods.[31,32] Further, mapping images in Fig. 1e exhibit that C, O and Zn elements presented a uniform spatial distribution on the carbon textile substrate. Notably, the distribution areas of C and Zn elements were highly consistent in diameter (Fig. 1f). This result proved that Zn-HHTP completely coated the surface of ZnO nanorods.

X-ray diffraction (XRD) analysis was conducted to elucidate the crystal structure of the synthesized materials. As depicted in Fig. 2a, the three characteristic diffraction peaks at 4.7°, 9.6° and 12.8° correspond to the (100), (200) and (210) crystal planes of the Zn-HHTP crystal,[24] respectively. The position of the (100) crystal plane is consistent with the calculated result of the 1.8 nm interplanar spacing observed by TEM, confirming the existence of Zn-HHTP crystals. In addition, the diffraction peaks at 31.6° and 34.2° in the XRD pattern correspond to the (100) and (002) crystal planes of hexagonal wurtzite ZnO (PDF#36-1452), respectively.[32–34] This result not only confirms the existence of ZnO nanorod arrays, but also strongly proves the successful composite of Zn-HHTP crystals on the surface of ZnO nanorod arrays. The precise matching of diffraction peak positions and intensities indicates that both crystal phases in the composite material maintain good crystalline quality.

X-ray photoelectron spectroscopy (XPS) analysis was carried out to explore the elemental chemical states of the Zn-HHTP@ZnO composite. As illustrated in Fig. 2b and c, the XPS survey spectrum reveals characteristic peaks exclusively for Zn, O and C indicating the compositional purity of the material. The C 1s spectrum exhibits three distinct valence states: the peak at 284.2 eV is assigned to quinone-type carbon (C=C) in the HHTP ligand, while the peaks at 285.9 eV and 288.3 eV correspond to C–O and C=O bonds, respectively.[35] In contrast, only the signals of the C–O and C=O bonds belonging to the carbon textile are observed in the C 1s spectrum of the ZnO sample (Fig. S2a), while the intensity of the C=O signal for the Zn-HHTP@ZnO sample increases significantly compared with that for the ZnO sample. In the O 1s spectrum (Fig. 2d), the peak at 530.8 eV originates from O–Zn bonds in ZnO, whereas the peaks at 532.0 eV and 533.8 eV are attributed to C–O and O=C bonds. In contrast, only the peak corresponding to the O–Zn bond is present in the ZnO sample (Fig. S2b).[36] The presence of the O=C bond provides direct evidence for the successful incorporation of Zn-HHTP. Finally, the Zn 2p spectrum (Fig. 2e) displays characteristic peaks at 1021.5 eV (Zn $2p_{3/2}$) and 1044.6 eV (Zn $2p_{1/2}$). This stable electronic configuration with fully occupied 3d orbitals facilitates the formation of robust coordination bonds with the HHTP ligand.[37,38] Thermogravimetric analysis (TGA) results of Zn-HHTP@ZnO and ZnO are shown in Fig. 2f. Both Zn-HHTP@ZnO with well-defined nanoarrays and pure ZnO exhibit exceptional thermal stability. Zn-HHTP completely decomposes into ZnO at around 450 °C, while the weight loss after 600 °C is attributed to the decomposition of the carbon textile. The reduced total weight loss rate of the Zn-HHTP@ZnO sample compared to pure ZnO indicates the successful loading of Zn-HHTP on the ZnO surface.

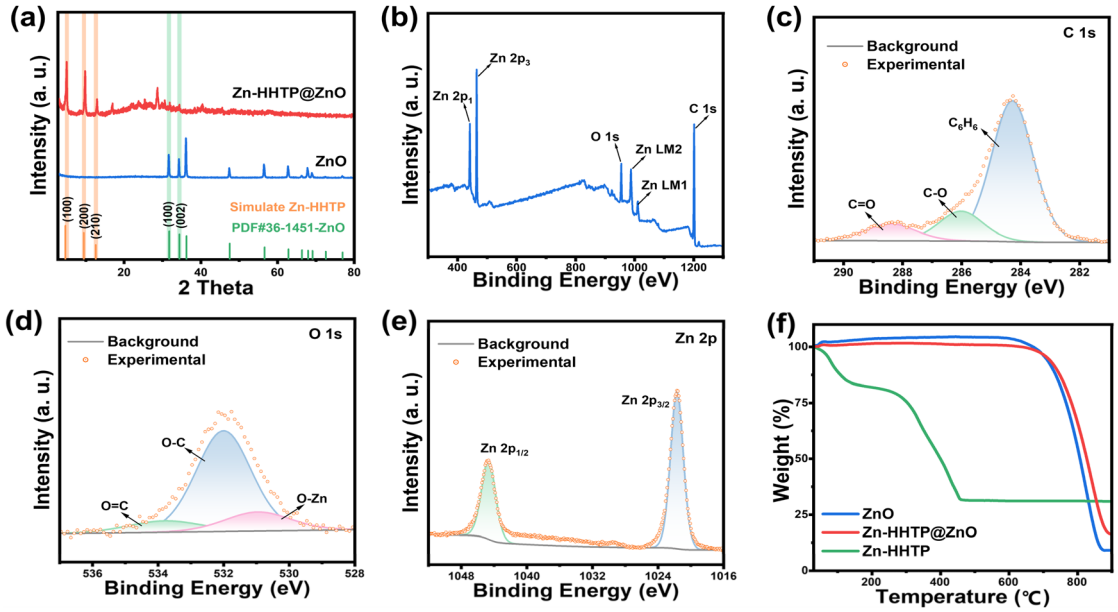

Fig. 2 (a) XRD patterns of Zn-HHTP@ZnO and ZnO. (b) XPS total spectrum of Zn-HHTP@ZnO. (c–e) C 1s, O 1s and Zn 2p spectra of Zn-HHTP@ZnO. (f) TGA curves of ZnO, Zn-HHTP@ZnO and Zn-HHTP.

The optical absorption properties were characterized by UV-visible spectroscopy. As shown in Fig. 3a and b, the Zn-HHTP composite exhibits a significantly broadened absorption range, with strong absorption in the ultraviolet region and an absorption edge extending into the near-infrared region ($\lambda > 800$ nm). The bandgaps of ZnO and Zn-HHTP were determined to be 2.95 eV and 1.35 eV, respectively, *via* linear extrapolation. Mott–Schottky measurements (Fig. 3c and S3) reveal that both ZnO and Zn-HHTP are n-type semiconductors with flat-band potentials of 1.89 V and 1.94 V, corresponding to conduction band positions of 1.69 V and 1.74 V, respectively. Combining the bandgap parameters, the valence band (VB) positions of Zn-HHTP and ZnO were calculated as 3.29 V and 4.84 V, respectively.

The photogenerated carrier dynamics of the samples were analyzed using PL and TR-PL spectra. In Fig. 3d, the Zn-HHTP@ZnO composite exhibits a weaker PL signal compared to ZnO, indicating a lower ratio and less photogenerated electron–hole pair recombination. Meanwhile, as shown in Fig. 3e, the average lifetime of Zn-HHTP@ZnO (0.42 ns) is shorter than that of ZnO (0.65 ns). The improved electron–hole separation ability was mainly attributed to heterojunction as illustrated in Fig. 3f, where the photogenerated holes can directly transfer from the CB of ZnO to that of Zn-HHTP avoiding recombination. The PL and TR-PL spectra collectively confirm that Zn-HHTP@ZnO exhibits better photocatalytic activity. This is beneficial for free electrons and holes to participate in redox reactions, improving their utilization efficiency and promoting the enhancement of photoassisted electrochemical performance. Furthermore, combined with the transient photocurrent response tests in Fig. 4, this indicates that after photogenerated carriers are produced under light irradiation, electrons in the Zn-HHTP@ZnO composite can be rapidly transferred through atomically grown Zn-HHTP to participate in the battery redox reactions, significantly suppressing electron–hole pair recombination.

The photocurrents of Zn-HHTP@ZnO and ZnO samples were further evaluated in a three-electrode system, where two pieces of metallic lithium served as the counter and reference electrodes. Zn-HHTP@ZnO and ZnO samples were used as photoelectrodes, with 1 M LiTFSI/TEGDME as the electrolyte. Before the test, the cell was purged with pure O_2 for 30 min. The transient photoresponse currents of Zn-HHTP@ZnO and ZnO cathodes are shown in Fig. 4a, b, S4a and b. During charging/discharging, Zn-HHTP@ZnO exhibits stable and stronger photocurrents than ZnO under full-spectrum light illumination, indicating higher charge separation efficiency. To systematically investigate the photoelectric response characteristics of photocathodes under different light illuminations, chopped light LSV and *i–t* tests were performed on Zn-HHTP@ZnO and ZnO cathodes under full-spectrum illumination, as well as specific wavelength (UV and visible) light irradiation. As shown in Fig. 4c, d and S5, the current density of Zn-HHTP@ZnO during charging demonstrates full-spectrum catalytic enhancement, with significantly improved visible light absorption compared to ZnO.

To further understand the photocurrent characteristics of Zn-HHTP@ZnO and ZnO, LSV and *i–t* tests were conducted under different wavelength illuminations to investigate the maximum photocurrent density and the relationship between photocurrent and light bands. As shown in Fig. 4e, f and S6–S8, both photocathodes exhibit the strongest current responses (3.27 mA cm^{-2} for Zn-HHTP@ZnO and 0.96 mA cm^{-2} for ZnO) under full-spectrum light illumination. Additionally, Zn-HHTP@ZnO generates current responses of 1.34 and 0.80 mA cm^{-2} under UV and visible light, respectively, far exceeding

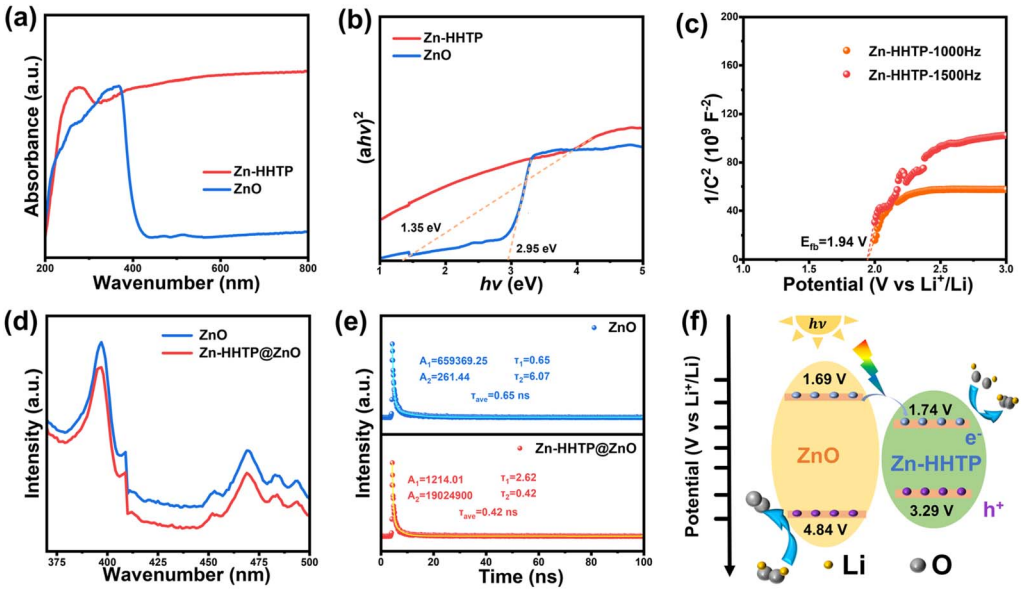

Fig. 3 (a and b) UV-visible spectra and corresponding Tauc plot curves of Zn-HHTP and ZnO. (c) Mott–Schottky curves of Zn-HHTP@ZnO. (d and e) Photoluminescence (PL) spectra and time-resolved PL spectra of Zn-HHTP@ZnO and ZnO. (f) Schematic illustration of the band structure and photogenerated charge-transfer process.

those of ZnO (0.16 and 0.08 mA cm^{-2}) and consistent with the PL and TR-PL spectral results in Fig. 3. Notably, the sum of responses in each band for both photocathodes is lower than the full-spectrum result, consistent with energy loss in photoelectric conversion. The results show that the photocurrent response of ZnO is significantly lower than that of Zn-HHTP@ZnO, relying mainly on UV light excitation. In contrast, Zn-HHTP@ZnO demonstrates enhanced visible light absorption, which outperforms that reported in previous related studies (Table S1), confirming that the heterostructure effectively improves carrier separation efficiency. This fully validates that the modification of conjugated Zn-HHTP not only broadens the light absorption range but also significantly enhances photocatalytic activity by optimizing interfacial charge transport.

The Zn-HHTP@ZnO sample was assembled into a non-aqueous LOB and first cycled at a current density of 0.02 mA cm^{-2} under different light conditions. As shown in Fig. 5a, the Zn-HHTP@ZnO sample provides a discharge plateau of 3.00 V and a charge plateau of 3.20 V under light illumination, yielding

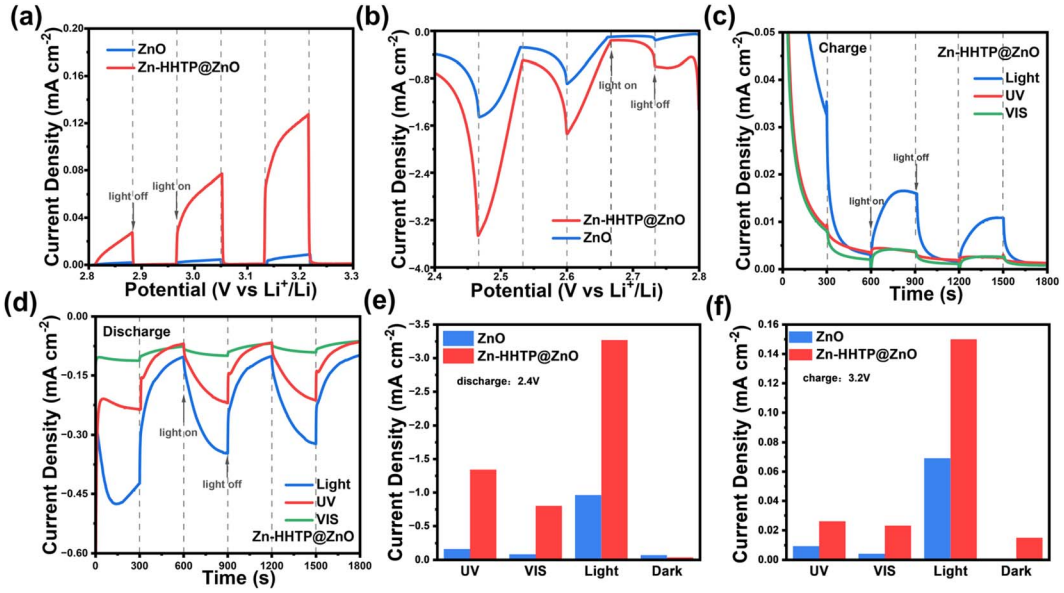

Fig. 4 Photoelectrochemical testing of Zn-HHTP@ZnO and ZnO cathodes. (a and b) LSV diagrams under chopped light. (c and d) *i*–*t* curves under chopped light at 3.0 and 2.6 V with different illumination (UV, visible and full spectrum). (e and f) The calculated discharge/charge photocurrent with different illumination.

a narrow polarization voltage of 0.20 V and an excellent energy efficiency of 93.4%, superior to that of previously reported photo-inspired LOBs (Table S2). This is attributed to the special band engineering process, which enables full-spectrum absorption to improve light energy utilization efficiency. Meanwhile, Zn-HHTP is tightly connected to ZnO that can rapidly transfer photogenerated carriers to the interface for reaction participation, thereby suppressing electron–hole pair recombination. Compared with ZnO, more electrons and holes are available for the redox reactions in Li–O_2 batteries, allowing the photoassisted Li–O_2 battery with the Zn-HHTP@ZnO photocathode to exhibit lower charge–discharge overpotentials and higher energy efficiency. To confirm the positive effect of illumination, discharge/charge measurements of the Zn-HHTP@ZnO sample were further conducted in the dark, where the discharge potential was 2.81 V and the charge potential was as high as 3.60 V, leading to an undesirable energy efficiency of 78%. After illumination, the charge potential of the Li–O_2 battery decreased by 0.40 V, demonstrating that illumination significantly promotes the decomposition of Li_2O_2. The redox performance differences of the Zn-HHTP@ZnO cathode under light/dark states were further analyzed by CV tests. As shown in Fig. 5b, illumination not only increases the ORR onset potential but also significantly enhances the redox current response, all of which indicate that light energy input has an obvious enhancement effect on the electrode reaction. In addition, electrochemical impedance spectroscopy (EIS) was used to analyze the charge transfer characteristics. As shown in Fig. 5c, the arc in the Nyquist plot corresponds to the charge transport process at the electrode/electrolyte interface, and its diameter directly reflects the interfacial impedance value. Under illumination, the arc diameter sharply decreases from 404.54 Ω in the dark state to 10.98 Ω, and this order-of-magnitude difference fully proves that photoexcitation can effectively improve the interfacial charge transfer efficiency.

Fig. 5d presents the results of the rate performance test of the Zn-HHTP@ZnO cathode under illumination, with a cut-off capacity of 0.08 mA h cm^{-2} and current densities increasing from 0.01 to 0.12 mA cm^{-2}. The discharge potentials of the battery based on the Zn-HHTP@ZnO cathode are 3.00, 3.00, 3.29, 2.87, and 2.48 V, with corresponding charge potentials of 3.18, 3.27, 3.4, 3.91, and 4.09 V. When the current density returns to 0.01 mA cm^{-2}, the discharge potential remains at 2.98 V with only slight decay, while the charge potential is 3.66 V, fully demonstrating the excellent rate retention capability of the electrode material. Further cycle tests (Fig. 5e) show that under illumination, the Li–O_2 battery with a Zn-HHTP@ZnO cathode exhibits an initial discharge potential of 3.00 V and charge potential of 3.20 V at a current density of 0.02 mA cm^{-2}. After 200 hours of cycling, the electrode maintains good electrochemical stability, with the discharge potential remaining at 2.91 V and the charge potential only increasing to 3.55 V. In contrast, the initial polarization voltage in the dark state is as high as 1.13 V (discharge 2.74 V/charge 3.87 V). In addition, the evaluation of long-term cycling and fast-charging performance is crucial for secondary batteries.[39,40] We conducted cycling performance tests at higher current densities (0.1 mA cm^{-2}) to evaluate the cycling and fast-charging performance of the photoassisted Li–O_2 battery with the Zn-HHTP@ZnO cathode (Fig. S9). At a high current density of 0.1

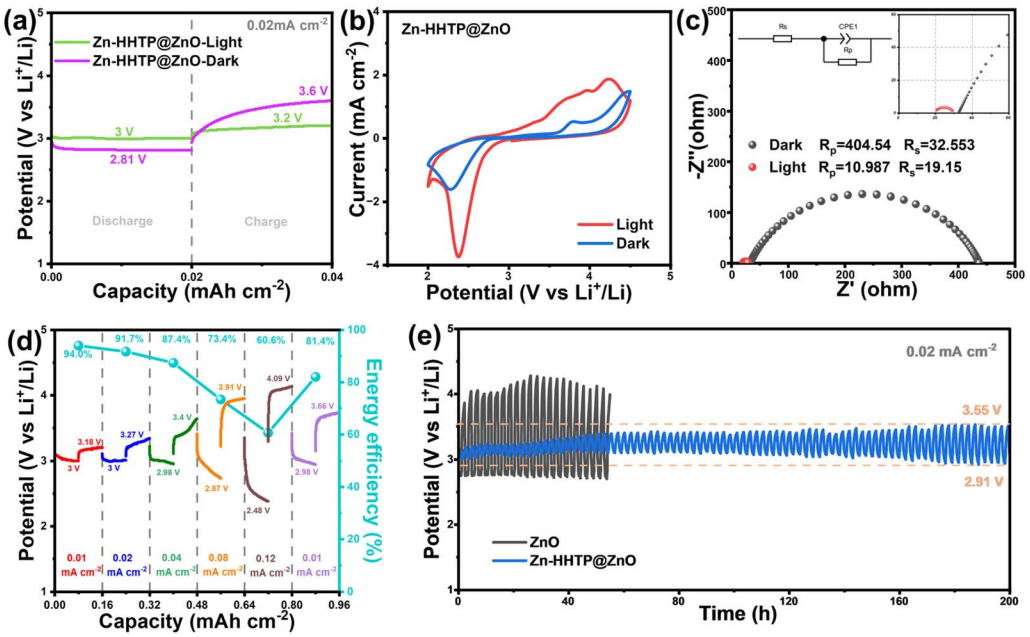

Fig. 5 Electrochemical performance test of Zn-HHTP@ZnO cathode in light/dark condition. (a) First discharge–charge curves of the battery at a current density of 0.02 mA cm^{-2}, with a capacity limit of 0.02 mA h cm^{-2}. (b) Cyclic voltammetry curves with a scan rate of 0.5 mV s^{-1}. (c) EIS graph. (d) Charge–discharge curves of Zn-HHTP@ZnO cathode at different current densities. (e) Comparison of cycling performance of Zn-HHTP@ZnO cathode under light/dark conditions.

mA cm^{-2}, it could stably cycle for 150 hours, with first-cycle polarization voltages of 0.9 V. Notably, the Li–O_2 battery assembled with a Zn-HHTP@ZnO photocathode exhibits a charging voltage of only 3.7 V under such a high current density, which is much lower than that of Li–O_2 batteries assembled with solid electrocatalysts.[41,42] Compared with traditional electrocatalysts, the developed Zn-HHTP@ZnO photocathode shows significant advantages, and its low polarization voltages under both small and large current densities confirm the high efficiency of the light-assisted catalytic system.

To confirm the mechanism and reversibility of the light-assisted battery reaction, systematic characterization of the electrode products after charging/discharging was conducted. The Zn-HHTP@ZnO cathode was subjected to charge–discharge treatments at different depths under illumination at a current density of 0.02 mA cm^{-2}. As shown in Fig. 6a–c, when discharged to 0.80 mA h cm^{-2}, the original nanorod structure on the electrode surface was partially covered by dense discharge products, but the nanorod morphology was still observable. Further discharging to 2 mA h cm^{-2} completely covered the nanorods with discharge products, making the original structure invisible. After charging to the same depth of 2 mA h cm^{-2}, the discharge products decomposed, and the nanorod morphology became clearly distinguishable. Compared with the original electrode (Fig. S10), only a small amount of film-like products remained on the surface.[43,44] Component analysis of the discharge products by XPS (Fig. 6d) revealed a characteristic binding energy of 55.4 eV in the Li 1s spectrum, which fully matches the standard spectrum of $Li_{i2}O_2$, confirming that the discharge product is Li_2O_2. These characterization results not only confirm that the formation and decomposition processes of Li_2O_2 in the light-assisted system are consistent with those in traditional Li–O_2 battery systems but also reveal the morphological evolution law of products during charge–discharge processes.

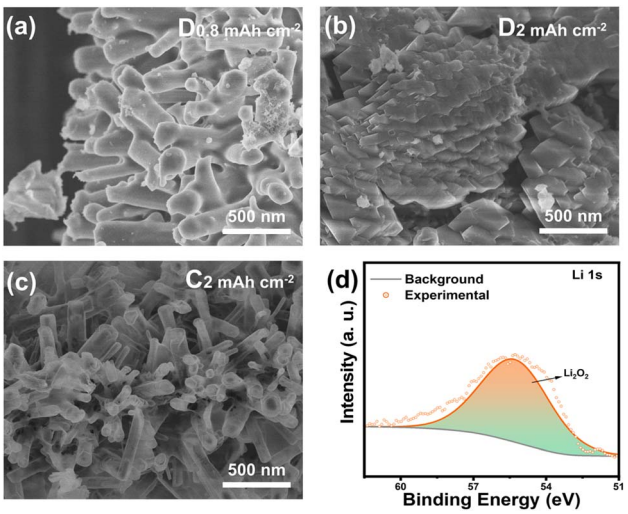

Fig. 6 (a and b) SEM images of Zn-HHTP electrodes at different discharge depths (0.8 mA h cm^{-2} and 2 mA h cm^{-2}). (c) SEM image of Zn-HHTP electrodes after charging to a depth of 2 mA h cm^{-2}. (d) Li 1s spectrum of the Zn-HHTP positive electrode discharged to 2 mA h cm^{-2}.

Conclusions

In this work, an *in situ* synthesized photocatalyst with nanorod array structure and abundant active catalytic sites is proposed. Its broad spectral response enables efficient light harvesting, and the generated charge carriers promote both ORR and OER. The nanorod-array-structured Zn-HHTP@ZnO composite effectively suppresses the recombination rate of photogenerated electrons and holes. Under illumination, the assembled LOBs exhibit a high discharge potential of 3.00 V and a low charge potential of 3.20 V, with a narrow overpotential of only 200 mV and a high energy efficiency of 93.4%. Sufficient photogenerated electrons ensure low discharge overpotential and uniform nucleation of discharge products. This study provides new insights for developing innovative, high-performance light-involved energy storage devices.

Author contributions

All authors have given approval to the final version of the manuscript.

Conflicts of interest

There are no conflicts to declare.

Data availability

All data needed to support the conclusions in the paper are presented in the paper and/or the supplementary information (SI) material. Additional data related to this paper may be requested from the corresponding author. Supplementary information: specific materials required for the experiment and sample preparation methods, SEM images of Zn-HHTP@ZnO, ZnO and Zn-HHTP electrodes, C 1s, O 1s XPS spectra ,Mott-Schottky curves of ZnO, *i–t* curve of Zn-HHTP@ZnO and ZnO cathodes under chopped light at 2.6 and 3.0 V in different light conditions, LSV diagram of Zn-HHTP@ZnO and ZnO cathodes under chopped light and different spectra, cycling performance of the Zn-HHTP@ZnO cathode under light illumination at current densities of 0.1 mA cm^{-2}, comparison of key performances between Zn-HHTP@ZnO and reported materials for enhancing ZnO's light absorption capacity, comparison of the electrochemical performances of Zn-HHTP@ZnO with reported cathode materials for Li–O_2 batteries. See DOI: https://doi.org/10.1039/d5sc06755c.

Acknowledgements

The authors express their appreciations for financial support from the National Science Foundations of China (22309084), the Natural Science Foundation of Jiangsu Province (BK20210616), the China Postdoctoral Science Foundation (2023M731589), and a project funded by the Priority Academic

Program Development of Jiangsu Higher Education Institutions (PAPD). H. R. Xue acknowledges support from the project of Zhongyuan Critical Metals Laboratory (GJJSGFYQ202422) and Zhongyuan Youth Talent Cultivation Project for Scientific and Technological Innovation.

Notes and references

1 H.-D. Lim, B. Lee, Y. Bae, H. Park, Y. Ko, H. Kim, J. Kim and K. Kang, Reaction chemistry in rechargeable Li-O_2 batteries, *Chem. Soc. Rev.*, 2017, **46**, 2873–2888.

2 Z.-L. Wang, D. Xu, J.-J. Xu and X.-B. Zhang, Oxygen electrocatalysts in metal-air batteries: from aqueous to nonaqueous electrolytes, *Chem. Soc. Rev.*, 2014, **43**, 7746–7786.

3 D. Aurbach, B. D. McCloskey, L. F. Nazar and P. G. Bruce, Advances in understanding mechanisms underpinning lithium–air batteries, *Nat. Energy*, 2016, **1**, 16128.

4 X. Chi, M. Li, J. Di, P. Bai, L. Song, X. Wang, F. Li, S. Liang, J. Xu and J. Yu, A highly stable and flexible zeolite electrolyte solid-state Li-air battery, *Nature*, 2021, **592**, 551–557.

5 H. Wang, X. Wang, M. Li, L. Zheng, D. Guan, X. Huang, J. Xu and J. Yu, Porous Materials Applied in Nonaqueous Li-O_2 Batteries: Status and Perspectives, *Adv. Mater.*, 2020, **32**, 2002559.

6 X. Wu, G. Meng, W. Liu, T. Li, Q. Yang, X. Sun and J. Liu, Metal-organic framework-derived, Zn-doped porous carbon polyhedra with enhanced activity as bifunctional catalysts for rechargeable zinc-air batteries, *Nano Res.*, 2018, **11**, 163–173.

7 Y. Wang, C. J. Zanelotti, X. Wang, R. Kerr, L. Jin, W. H. Kan, T. J. Dingemans, M. Forsyth and L. A. Madsen, Solid-state rigid-rod polymer composite electrolytes with nanocrystalline lithiumion pathways, *Nat. Mater.*, 2021, **20**, 1255–1263.

8 W.-J. Kwak, Rosy, D. Sharon, C. Xia, H. Kim, L. R. Johnson, P. G. Bruce, L. F. Nazar, Y.-K. Sun, A. A. Frimer, M. Noked, S. A. Freunberger and D. Aurbach, Lithium–Oxygen Batteries and Related Systems: Potential, Status, and Future, *Chem. Rev.*, 2020, **120**, 6626–6683.

9 D. Wang, X. Mu, P. He and H. Zhou, Materials for advanced Li-O_2 batteries: Explorations, challenges and prospects, *Mater. Today*, 2019, **26**, 87–99.

10 H. Song, H. Deng, C. Li, N. Feng, P. He and H. Zhou, Advances in Lithium-Containing Anodes of Aprotic Li-O_2 Batteries: Challenges and Strategies for Improvements, *Small Methods*, 2017, **1**, 17100135.

11 J. Lu, L. Li, J.-B. Park, Y.-K. Sun, F. Wu and K. Amine, Aprotic and Aqueous Li–O_2 Batteries, *Chem. Rev.*, 2014, **114**, 5611–5640.

12 Y. Ma, H. Qu, Z. Chi, X. Liu, Y. Yu, Z. Guo and L. Wang, The highly dispersed Co-based nanoparticles encapsulated into porous N-doping carbon polyhedral with the low content of Ru modification as a promising cathode catalyst for long-life Li-O_2 batteries, *Nano Res.*, 2022, **15**, 3204–3212.

13 X. X. Wang, D. H. Guan, F. Li, M. L. Li, L. J. Zheng and J. J. Xu, Magnetic and Optical Field Multi-Assisted Li-O_2 Batteries with Ultrahigh Energy Efficiency and Cycle Stability, *Adv. Mater.*, 2021, **34**, 2104792.

14 Z. Zhu, Y. Ni, Q. Lv, J. Geng, W. Xie, F. Li and J. Chen, Surface plasmon mediates the visible light-responsive lithium–oxygen battery with Au nanoparticles on defective carbon nitride, *Proc. Natl. Acad. Sci. U. S. A.*, 2021, **118**(17), e2024619118.

15 Q. Lv, Z. Zhu, S. Zhao, L. Wang, Q. Zhao, F. Li, L. A. Archer and J. Chen, Semiconducting Metal-Organic Polymer Nanosheets for a Photoinvolved Li-O_2 Battery under Visible Light, *J. Am. Chem. Soc.*, 2021, **143**, 1941–1947.

16 M. Li, X. Wang, F. Li, L. Zheng, J. Xu and J. Yu, A Bifunctional Photo-Assisted Li-O_2 Battery Based on a Hierarchical Heterostructured Cathode, *Adv. Mater.*, 2020, **32**, 1907098.

17 D. H. Guan, X. X. Wang, M. L. Li, F. Li, L. J. Zheng, X. L. Huang and J. J. Xu, Light/Electricity Energy Conversion and Storage for a Hierarchical Porous In_2S_3@CNT/SS Cathode towards a Flexible Li-CO_2 Battery, *Angew. Chem., Int. Ed.*, 2020, **59**, 19518–19524.

18 M. Yu, X. Ren, L. Ma and Y. Wu, Integrating a redox-coupled dye-sensitized photoelectrode into a lithium–oxygen battery for photoassisted charging, *Nat. Commun.*, 2014, **5**, 5111.

19 H. Gong, T. Wang, K. Chang, P. Li, L. Liu, X. Yu, B. Gao, H. Xue, R. Ma, J. He and J. Ye, Revealing the illumination effect on the discharge products in high-performance Li-O_2 batteries with heterostructured photocatalysts, *Carbon Energy*, 2022, **4**, 1169–1181.

20 G. Wang, X. Hu, J. Wang, Y. Wang, Y. Dou, M. Guo, Q. Zhang, J. Han, Z. Xie and Z. Zhou, Toward Practical Photo-Assisted Li-O_2 Batteries: a Four-Electron Pathway Enabled by Ru-Doped β-MnO_2, *Adv. Mater.*, 2025, **37**, 2507891.

21 B. Wen, Y. Huang, Z. Jiang, Y. Wang, W. Hua, S. Indris and F. Li, Exciton Dissociation into Charge Carriers in Porphyrinic Metal-Organic Frameworks for Light-Assisted Li-O_2 Batteries, *Adv. Mater.*, 2024, **36**, 2405440.

22 R. Cao, Y. Cui, G. Huang, W. Liu, J. Liu and X. Zhang, Designing a photo-assisted Co-C_3N_4 cathode for high performance Li-O_2 batteries, *Nano Res.*, 2023, **16**, 8405–8410.

23 H. Xue, H. Gong, Y. Yamauchi, T. Sasaki and R. Ma, Photo-enhanced rechargeable high-energy-density metal batteries for solar energy conversion and storage, *Nano Res. Energy*, 2022, **1**, 9120007.

24 E. Z. Zhu, X. Shi, G. Fan, F. Li and J. Chen, Photo-energy Conversion and Storage in an Aprotic Li-O_2 Battery, *Angew. Chem., Int. Ed.*, 2019, **58**, 19021–19026.

25 T. Slimani Tlemcani, C. Justeau, K. Nadaud, G. Poulin-Vittrant and D. Alquier, Deposition Time and Annealing Effects of ZnO Seed Layer on Enhancing Vertical Alignment of Piezoelectric ZnO Nanowires, *Chemosensors*, 2019, **7**, 7.

26 H. J. Jung, S. Lee, Y. Yu, S. M. Hong, H. C. Choi and M. Y. Choi, Low-temperature hydrothermal growth of ZnO nanorods on sol–gel prepared ZnO seed layers: Optimal growth conditions, *Thin Solid Films*, 2012, **524**, 144–150.

27 M. A. Asmadi, A. A. M. Ralib, N. B. Saidin and A. N. Nordin, Optimization of hydrothermally grown ZnO nanorods on flexible fabric using finite element simulation and single precursor for wearable nanogenerator, *J. Mater. Sci.: Mater. Electron.*, 2024, **35**, 2244.

28 A. A. M. Raub, R. Bahru, S. N. A. M. Nashruddin and J. Yunas, A review on vertical aligned zinc oxide nanorods: Synthesis methods, properties, and applications, *J. Nanopart. Res.*, 2024, **26**, 186.

29 A. Y. Al-She'irey, A. Balouch, E. R. Mawarnis, L. Roza, M. Y. A. Rahman, Abdullah and A. M. Mahar, Effect of ZnO seed layer annealing temperature on the growth of ZnO nanorods and its catalytic application, *Opt. Mater.*, 2022, **131**, 112652.

30 K. Liu, M. Zhang, X. Du, A. Zhou, B. Hui, Y. Xia and K. Zhang, Zinc-catecholete frameworks biomimetically grown on marine polysaccharide microfibers for soft electronic platform, *Nano Res.*, 2023, **16**, 1296–1303.

31 Y. Jin, T. Zhang, N. Pan, S. Wang, B. Zhang, X. Zhu, Y. Hao, X. Wang, L. Song and M. Zhang, Surface functionalization of carbon cloth with conductive Ni/Fe-MOFs for highly efficient oxygen evolution, *Surf. Interfaces*, 2022, **33**, 102294.

32 N. Ekthammathat, T. Thongtem, A. Phuruangrat and S. Thongtem, Growth of hexagonal prism ZnO nanorods on Zn substrates by hydrothermal method and their photoluminescence, *Ceram. Int.*, 2013, **39**, S501–S505.

33 L. Tang, X.-B. Bao, H. Zhou and A.-H. Yuan, Synthesis and characterization of ZnO nanorods by a simple single-source hydrothermal method, *Phys. E*, 2008, **40**, 924–928.

34 A. Rana, R. Malik, M. Rana, D. Kaushik, S. P. Khanna, R. Srivastava and C. K. Suman, Studies of optoelectrical properties of Mn-doped ZnO nanostructure for supercapacitor and photodetector applications, *J. Alloys Compd.*, 2024, **997**, 174931.

35 X. Chen, Y. Chen, L. Zhang, Z. Liu, E. Qiu, Q. Liu, M. D. Regulacio, C. Lin and D.-P. Yang, Hydrophilic ZnO/C nanocomposites with superior adsorption, photocatalytic, and photo-enhanced antibacterial properties for synergistic water purification, *J. Colloid Interface Sci.*, 2023, **648**, 535–550.

36 G. P. Singh and M. K. Roy, Structural and optical study of high concentrate Co-doped ZnO nanostructures, *Mater. Today: Proc.*, 2021, **46**, 5852–5856.

37 A. Latif, L. Arab, A. Amri, H. Arab, N. Sengouga and T. Tibermacine, Effect of Ga doping on the structural, optical, and electrical properties of ZnO nanopowders elaborated by sol-gel method, *Mater. Res. Bull.*, 2024, **178**, 112886.

38 Y. Jin, X. Yuan, L. Ou, J. Wu, J. Hu, K. Xue and X. Xiong, In situ fast self-assembled preparation of dandelion-like $Cu(OH)_2@Cu_3(HHTP)_2$ with core-shell heterostructure arrays for electrochemical sensing of formaldehyde in food samples, *Food Chem.*, 2024, **447**, 139013.

39 J. Mun, T. Song, M. S. Park and J. H. Kim, Paving the Way for Next-Generation All-Solid-State Batteries: Dry Electrode Technology, *Adv. Mater.*, 2025, **37**, 2506123.

40 J. H. Suh, S. A. Han, S. Y. Yang, J. W. Lee, Y. Shimada, S. M. Lee, J. W. Lee, M. S. Park and J. H. Kim, Toward Fast-Charging and Dendritic-Free Li Growth on Natural Graphite Through Intercalation/Conversion on MoS2 Nanosheets, *Adv. Mater.*, 2025, **37**, 2414117.

41 Y. Yang, X. Hu, G. Wang, J. Han, Q. Zhang, W. Liu, Z. Xie and Z. Zhou, Two Better Than One: Enhanced Photo-Assisted Li-O_2 Batteries with Bimetallic Fe-UiO-66 Metal-Organic Framework Photocathodes, *Adv. Funct. Mater.*, 2024, **34**, 2315354.

42 Y. Tao, X. Fan, X. Yu, K. Gong, Y. Xia, H. Gong, H. Chen, X. Huang, A. Zhang, T. Wang and J. He, Metal–Organic Framework with Dual Excitation Pathways as Efficient Bifunctional Catalyst for Photo-assisted Li–O_2 Batteries, *Small*, 2024, **20**, 2403683.

43 J. M. Garcia-Lastra, J. D. Bass and K. S. Thygesen, Communication: Strong excitonic and vibronic effects determine the optical properties of Li_2O_2, *J. Chem. Phys.*, 2011, **135**, 121101.

44 M. Wang, J. Chen, Z. Tian, W. Dai, B. Cui, X. Cui, D. Wang, Y. Xiao, X. Lian, C. Jiang, H. Yang, Y. Wang, Z. Sun, Y. Ding, Y.-Y. Sun, J. Zhang and W. Chen, Facet-controlled bifunctional WO3photocathodes for high-performance photo-assisted Li–O_2 batteries, *Energy Environ. Sci.*, 2023, **16**, 523–534.